Supplementary Information

Salt-rejecting Anisotropic Structure for Efficient Solar Desalination via Heat-mass Flux Decoupling

This PDF file includes:

different temperatures.

Fig. S4 Schematic diagram of solar desalination setups and infrared images of solar evaporation **process**.

Fig. S5 Hypsometric map of solar evaporation performance.

Fig. S6 Digital photos of water flux direction test.

Fig. S7 Geometric setups of finite simulation models.

Fig. S8 Schematic diagram of heat transfer process within HSI after 20 ms.

Fig. S9 Schematic diagram of heat transfer process within VSI after 20 ms.

Fig. S10 Schematic diagram of heat transfer process within VSI after 20 ms.

Fig. S11 Images of VSI surface after 1-hr solar desalination.

Table S1 Literature Comparisons.

S1. Characterization

Since the anisotropy was closely related to the micro-structure, we prepared the sugarcane-derived anisotropic structure in different ways according to the growth direction (Fig. S1): (1) horizontally (perpendicular to the growth direction) cut sugarcane internodes (HSI-*x*), (2) vertically (parallel to the growth direction) cut sugarcane internodes (VSI-*x*), (3) horizontally cut sugarcane nodes (HSN-*x*), where *x* represents the pyrolysis temperatures of 400, 700, 900 ˚C respectively. Among the aforesaid three types structures, HSI and HSN shared similar vertically penetrated structures while VSI was horizontally penetrated.

Surface elemental analyses by X-ray photoelectron spectroscopy (XPS) showed that hydrothermal treatment had preliminarily carbonized the sugarcane (Fig. S2a). Following calcination and higher calcination temperatures further lowered the O element (both C=O and C-O) percentage, and C-C dominated the composition of VSI, HSI and HSN (Fig. S2c-d). Consistently, FT-IR spectrum also showed that three different structures after hydrothermal treatment still showed -OH, -C=O and -C-O vibrations while -OH vibration disappeared after pyrolysis (Fig. S3a). Moreover, ALS-900 only exhibited strong absorption in fingerprint area and no -OH vibration was detected.

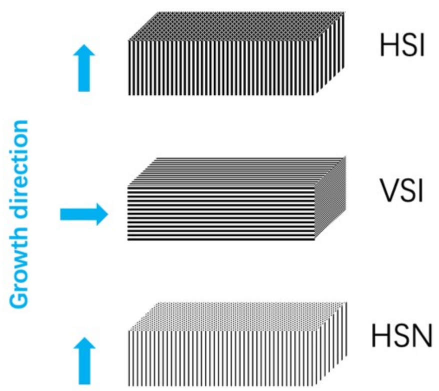

Fig. S1 Schematic diagram of different ALSs.

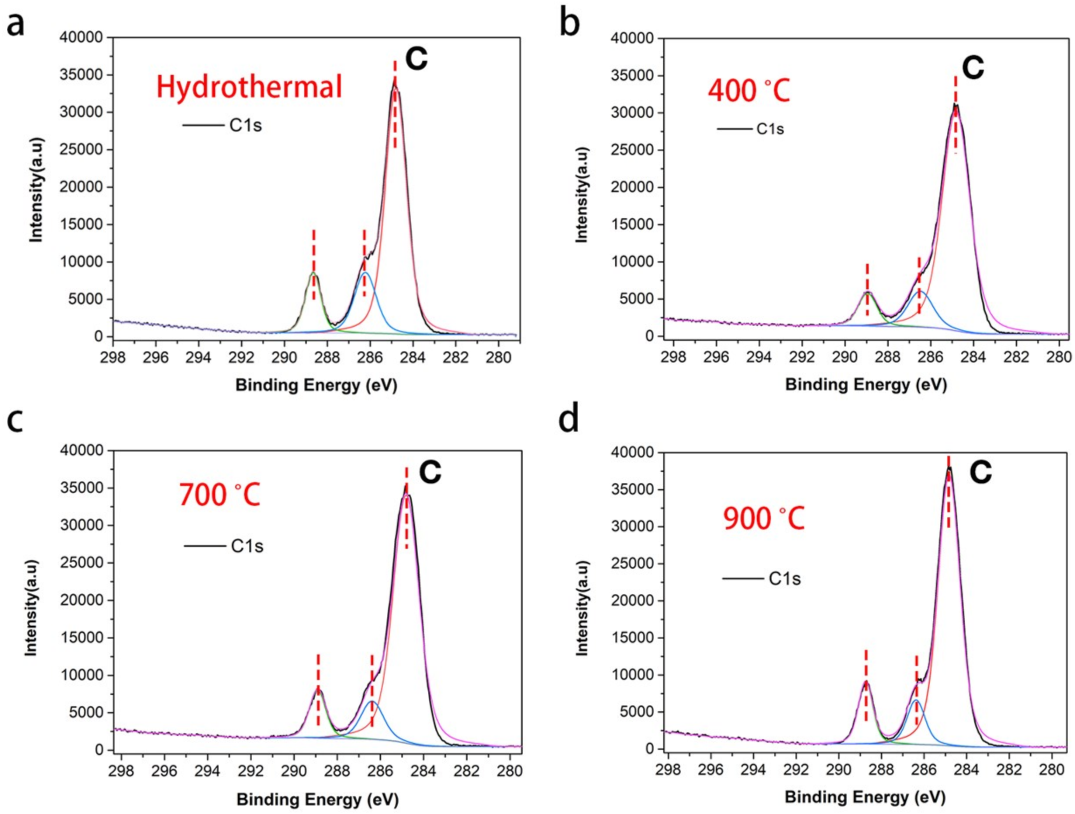

Fig. S2 XPS spectrum of sugarcane after hydrothermal and pyrolyzation of different temperatures.

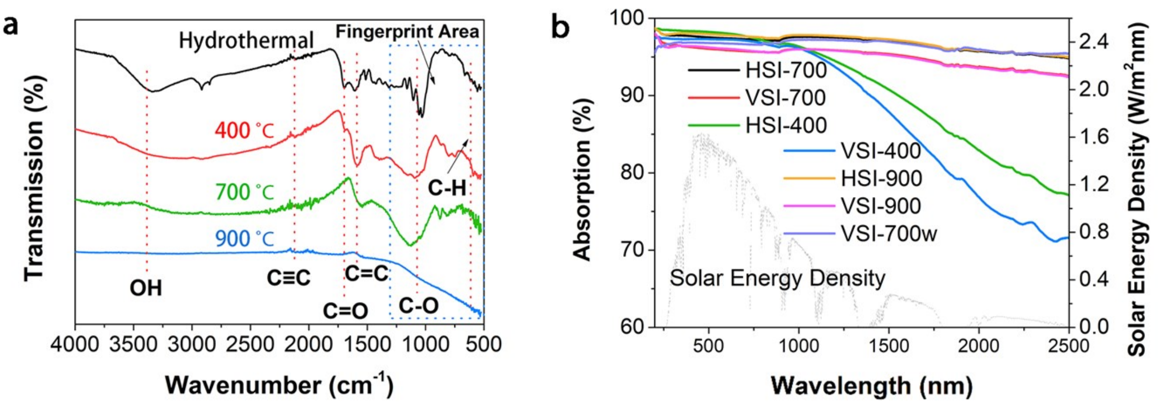

Fig. S3 a) FT-IR image of sugarcane after hydrothermal and pyrolyzation of different temperatures. b) UV-vis spectrum of VSI, HSI and HSN.

S2. Efficiency and energy conservation calculation

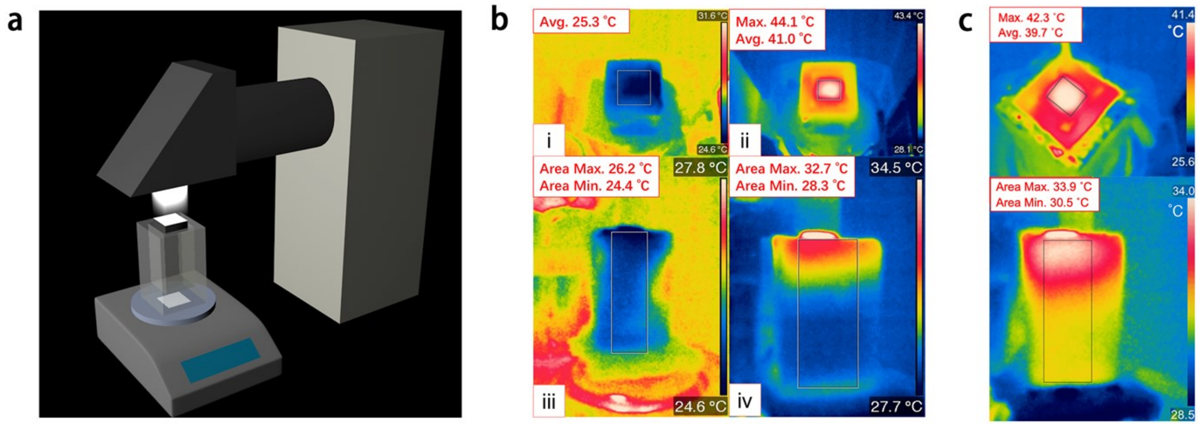

Fig. S4 Characterization of the solar steam generation efficiency of VSI-700 and HSI-700. (a) Schematic diagram of solar desalination setups and (b) Infrared images of solar evaporation process for VSI-700 (i and ii, the sugarcane surface; iii and iv, profile of bulk water before and after 1-hour one sun irradiance, respectively). (c) Infrared images of solar evaporation process for HSI-700 after 1-hour one sun irradiance.

According the equation of phase-change enthalpy ($h_{pc} = 1918.46 \times [T/(T-33.91)]^2$ kJ kg^{-1}) and the average surface temperature (41 °C) shown in Fig. S4,

$$h_{pc\ 41^{\circ}C} = 1918.46 \times \left(\frac{314.15}{314.15 - 33.91}\right)^2 = 2410\ \text{kJ kg}^{-1}$$

The efficiency of VSI-700 can be calculated as:

$$\eta_{evp}\% = \frac{\dot{m}(h_s + h_{pc})}{q_{solar}}\% = \frac{(\dot{m}_{obs} - \dot{m}_{background}) \times (h_s + h_{pc})}{q_{solar}} = \frac{(1.05 \pm 0.05) \times (4}{1 \times 30} \quad 86.5\% \pm 4\%$$

To verify the energy conservation, the heat loss in different forms are listed as follows:

$$\dot{m}h_{LV} = \alpha q_{solar} - \varepsilon\sigma\left(T^4 - T_{\infty}^4\right) - h(T - T_{\infty}) - q_{water}$$

S2.1 Light absorbing loss

Light absorbing process defines the total heat energy input of the system. According to the UV-Vis spectrum of aerogel-like sugarcane carbon, light absorbance is ~97%. So $\alpha q_{solar} > 970\ W/m^2$, and it accounts for 3% of total energy.

S2.2 Radiative heat loss

For radiative heat loss, T is defined as the average temperature of evaporation surface (41˚C), and T_∞ is the temperature of air above VSI. However, VSI surface is surrounded with hot water vapor,[1] which is measured to be ~ 38.2 ˚C. It prevents it from direct contact with cold air (26 ˚C). According to Kirchhoff law, ε is defined as 0.97, then radiative heat loss is estimated to account for 1.9% of total energy.

S2.3 Convective heat loss

For convection heat loss, heat transfer coefficient h is calculated as follows:

$$h = \frac{C \cdot Ra^n}{D} \cdot \lambda$$

$$Ra = Gr \cdot Pr = \frac{Gr \cdot \beta \cdot g \cdot \rho^2 \cdot D^3 \cdot \Delta T}{\mu^2}$$

Gr is the Grashof number of the air, C and n are coefficients, g is gravity constant, ρ is the density of air, μ represents the dynamic viscosity of air, D is the characteristic size of material, ΔT represents the temperature differences between the evaporation surface and the ambient air. During the evaporation process, the water vapor (38.2 ˚C) generated and will directly heated up the air above the material and hinder the cold air (26 ˚C) from getting close to the evaporation surface to get heated.[1, 2] Thus, the convective heat loss was greatly minimized.

As a result, ΔT is estimated as 2.8 K, thus h is estimated as 7.55 W/(m^2·K), and convective heat loss is calculated to account for 2.1% of total absorbed energy.

S2.4 Conductive heat loss

Conduction heat loss is estimated by the temperature gradient in bulk water.

$$q_{water} = k\Delta T/\Delta l$$

A is the conduction area and k is the thermal conductivity of bulk water. ΔT represents the temperature change of bulk water, Δl is the 20 mm. As monitored, the temperature changes of upper water and bulk water are 1.76 and 0.38 K. Thus, conductive heat loss is calculated to account for 4.5% of total energy.

In conclusion, all the energy loss sums up to be 11.5%, which is in well agreement with the calculated solar evaporation efficiency of 86.5%±4%.

Likewise, the energy balance of HSI-700 can be analyzed. The energy loss for HSI-700 mainly comprised of 2.5% light absorbing loss, 1.9% radiative heat loss, 2.2% convective heat loss and 11.64% conductive heat loss, which summed up to be 18.24 % and agreed with the calculated evaporation efficiency of 79.8% ± 1.2%.

Therefore, the light absorbing loss, radiative loss and convective loss of VSI-700 and HSI-700 were similar. VSI effectively suppressed conductive heat loss to the bulk water, so its solar evaporation efficiency was elevated.

S2.5 Solar evaporation performance comparison

To further clarify the tendencies, hypsometric maps as a function of both structure and composition were drawn. VSI-700 clearly emerged as the hot spot for solar evaporation (Fig. S5). Even though higher calcination temperatures led to better solar absorption (Fig. S5c), solar evaporation performance still first increased and then decreased, proving that the utilization of absorbed energy within different structures governed the solar evaporation efficiency. Generally, higher calcination temperature led to a slight shrinkage of the ALS skeleton and thus a higher water content when floating on the water (Fig. S5b). Since optimal water content has been reported to be beneficial for heat management and solar evaporation,[2-5] the moderate water content of VSI is in accordance with its preferred solar evaporation performance when compared to HSI and HSN calcinated under the same temperature. However, the solar evaporation performance rose to a higher level with a much higher water content for VSI, indicating that a horizontally penetrated structure is a better option for solar evaporation than a vertically penetrated one (Fig. S5a). Specifically, beyond the influence of water content, the totally different ways of mass and energy transfer were inferred to account for the optimal solar evaporation performance of VSI.

Besides, both VSI and HSI with different sicknesses have been investigated. As shown in Fig. S5d, with the sickness increasing, the net evaporation rate of both VSI and HSI were boosted, indicating promoted solar evaporation efficiencies. Interestingly, the increasement of the net evaporation rate exhibited different features, where the increasements were less dramatic for VSI compared to that of HSI. As reported, thicker solar evaporators (thicker heat insulating layer) led to more efficient heat localization at the evaporation surface.[6] This suggested that the heat loss in VSI was better minimized than in HSI, so VSI did not rely on increasing its thickness to achieve better heat localization effect. In addition, no observable salt precipitated for all VSI and HSI samples with different samples, demonstrating efficient salt diffusion in them.

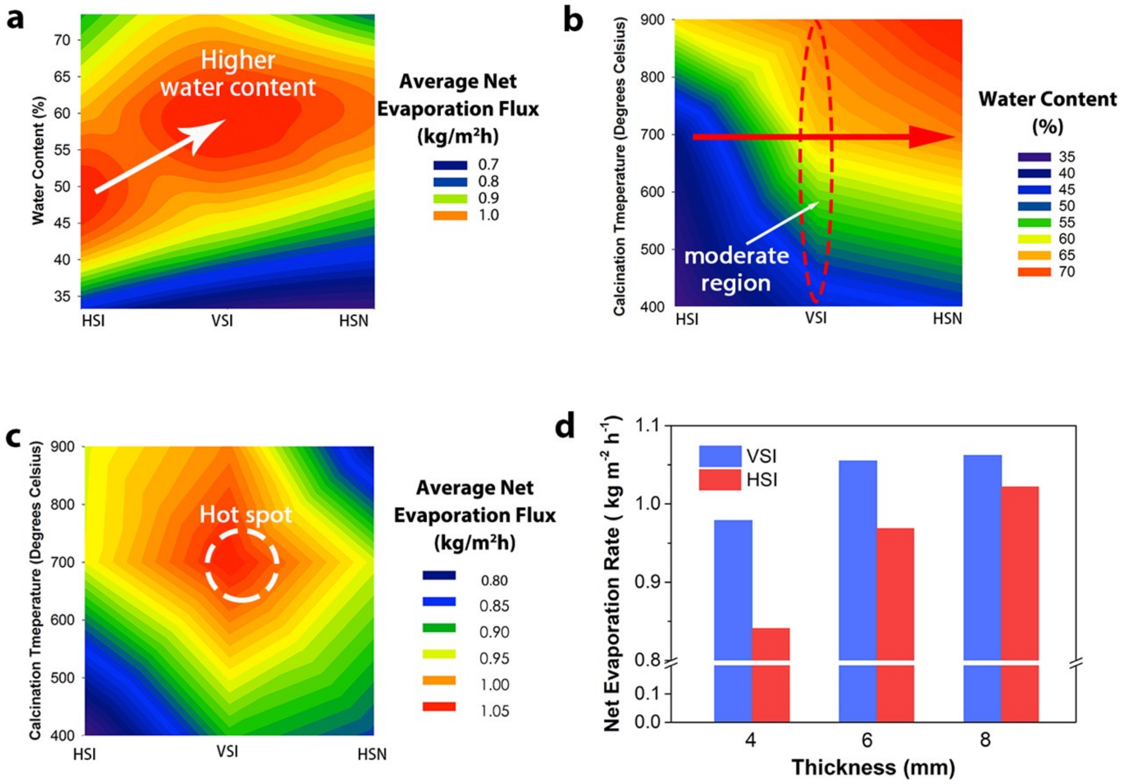

Fig. S5 Comparisons between different anisotropic structures. (a) Solar evaporation performance as a function of calcination temperatures and structures. (b) Water content as a function of calcination temperatures and structures. (c) Solar evaporation performance as a function of calcination temperatures and structures. (d) Comparison of the net evaporation rate between HSI-700 and VSI-700 with different thicknesses.

S3. Water and salt transfer path identification

Since HSI and HSN shared similar micro-unit but worked in different directions when compared to VSI, HSI and VSI with the same sickness of 6 mm were chosen to compare the water flux rate in them. The depth of both pure water and $FeCl_3$ solution were controlled at 2 mm to ensure that only bottom part of HSI and VSI are in direct touch with the liquids. Therefore, capillary flow is needed for liquids transport from the bottom of materials to their top surface. As depicted in Fig. S6, after soaking in pure water for 40 s, the bibulous paper in touch with the top surface of VSI started to become wet (Fig. S6a), which is clearer in $FeCl_3$ solution (Fig. S6b, c). Differently, for HSI, it only took 6 s for the liquids transport from the bottom of HSI to its top surface (Fig. S6e-f). This difference clearly demonstrated the water transport rate was much faster in vascular bundles, which was horizonal in VSI while vertical in HSI. Thus, water flux is mainly provided horizontally for VSI while vertically for HSI, which was later used as the proof for the two laminar flow inlets (Fig. 3a) for numerical simulation models.

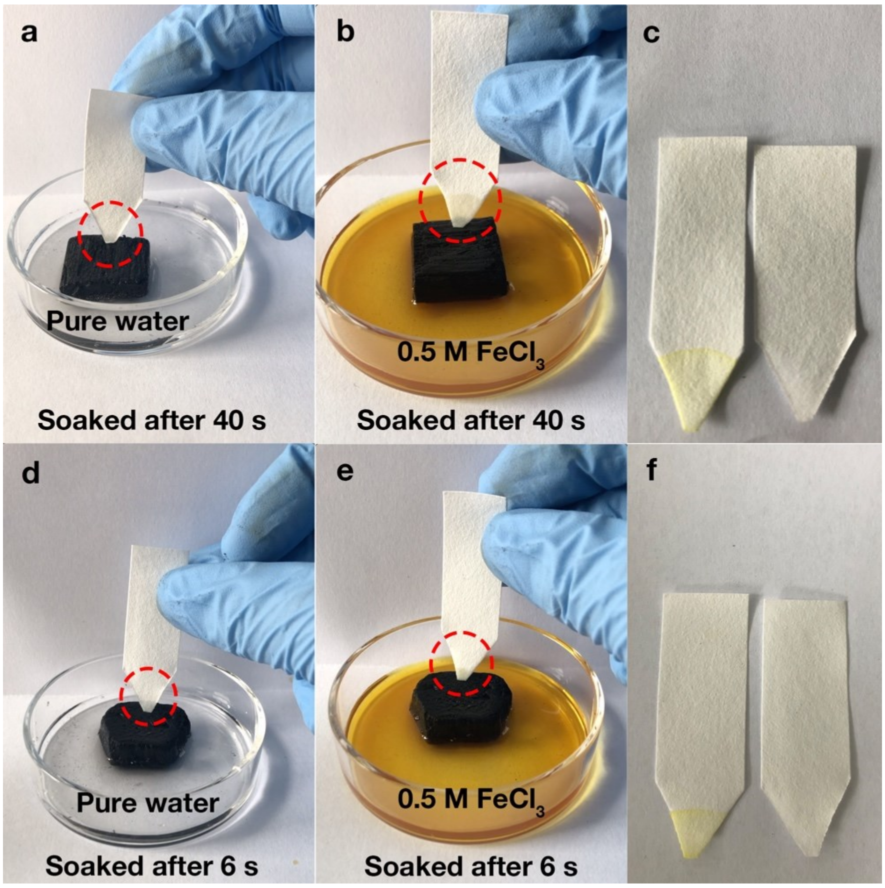

Fig. S6 Digital photos of water flux direction test. (a-c) VSI soaked in pure water, $FeCl_3$ solution, and the conditions of bibulous paper, respectively. (d-f) HSI soaked in pure water, $FeCl_3$ solution, and the conditions of bibulous paper, respectively.

S4. Numerical simulation setups

To clearly illustrate the upper limit of heat and salt transfer in water path, one 3D model was set up. It was a simple unit with the same volume of water as HSI and VSI. It follows all the setups in ht and tds modules in numerical simulation setups. However, in spf module, no water velocity field was applied to rule out the impact of water flow.

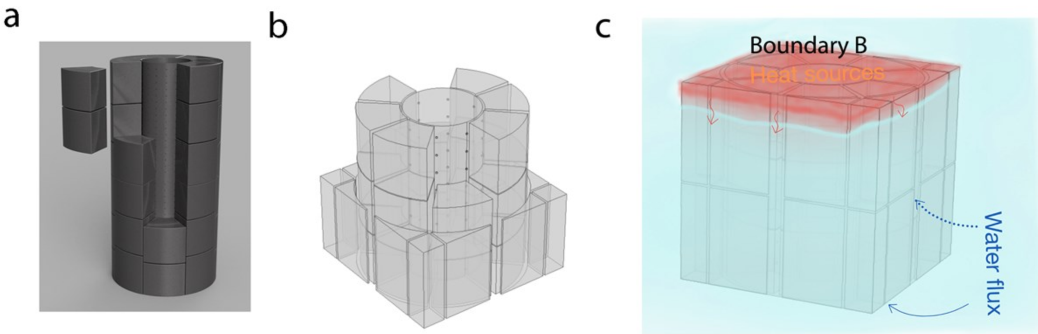

Fig. S7 Geometric setups of finite simulation models. (a) Anisotropic structure of sugarcane based on SEM images. (b) Inner structure of the geometric model. (c) Schematic diagram of HSI model.

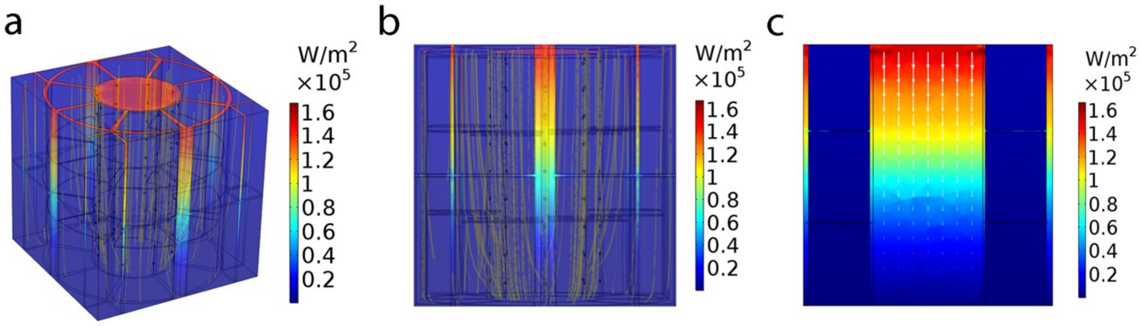

Fig. S8 Schematic diagram of heat transfer process within HSI after 20 ms. (a, b) 3D (a) and profile (b) display (yellow lines represent heat flux distribution). (c) Profile display (white lines represent heat flux direction).

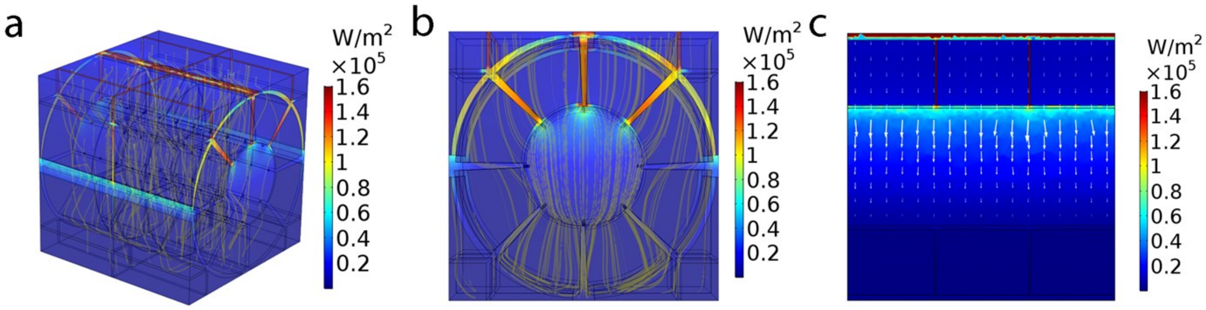

Fig. S9 Schematic diagram of heat transfer process within VSI after 20 ms. (a, b) 3D (a) and profile (b) display (yellow lines represent heat flux distribution). (c) Profile display (white lines represent heat flux direction).

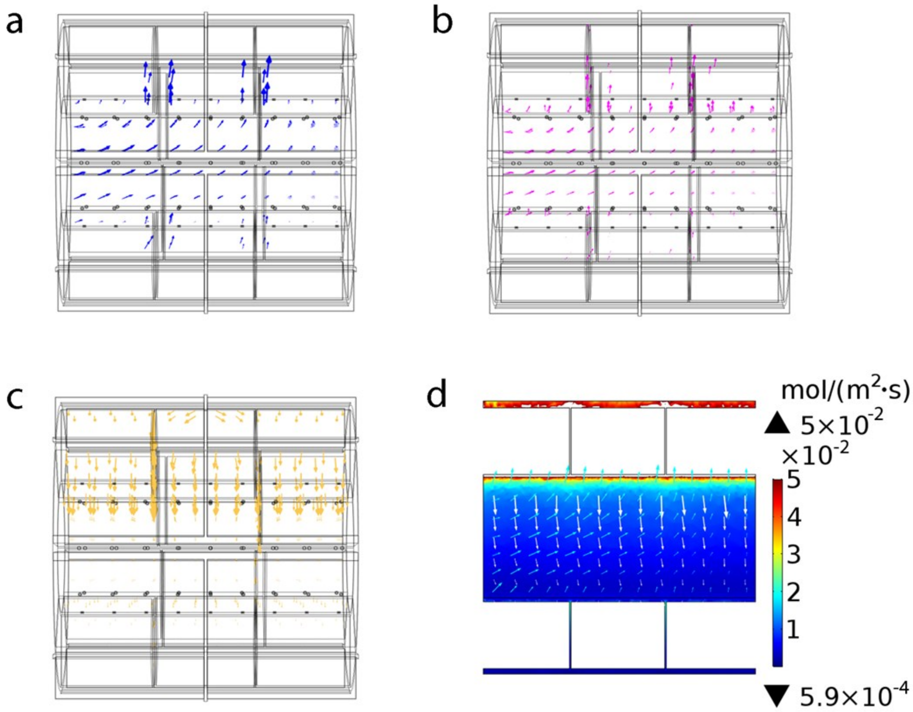

Fig. S10 Schematic diagrams of the coupling between salt flux and water transportation in VSI. (a) Streamlines of water transportation within VSI. (b) Streamlines of salt flux induced by convection. (c) The Streamlines of salt flux induced by concentration diffusion. (d) Total salt flux intensity in rainbow colors and total salt flux arrows after salt dispersion for 10 seconds.

S5 Solar desalination

S5.1 Slat-rejecting property

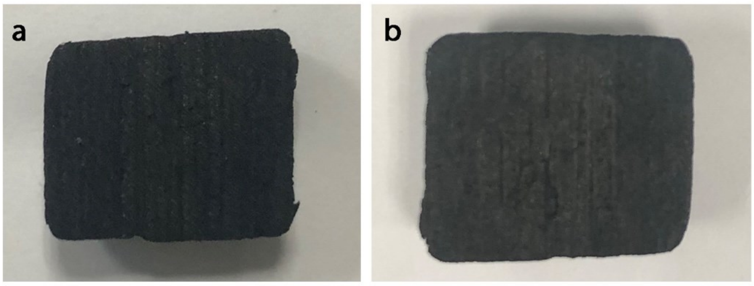

Fig. S11 Images of VSI surface after 1-hr solar desalination under 2-sun (a) and 3-sun (b) irradiance.

Table S1 Literature Comparison

References	Material Descriptions	Efficiency (%)			
		Direct Contact	Partial Direct Contact	Capillary Water Flow	Confined Water Flow
2016 Nature Photonics[7]	AAO single layer	<60	-	-	-
2015 Nature Communication[8]	Thin-film black gold membranes	<40	-	-	-
2017 Acs Nano[9]	Functionalized graphene membrane	48%	-	-	-
2016 Science Advances[10]	Gold nanoparticles deposited on AAO membrane	60-65	-	-	-
2017 Advanced Materials[11]	3D-printed CNT/GO layer & GO/NFC layer	-	-	-	85.6
2018 Nature Nanotechnology[4]	A hierarchically nanostructured gel	-	-	94	-
2018 Advanced Energy Materials[12]	Monolithic Hollow-Carbon-Nanotubes Aerogels	-	-	86.8	-
2017 Advanced Materials[13]	Carbon of mushrooms	-	-	78	-
2015 Advanced Materials[14]	Porous Graphene	-	-	80	-

2018 Acs Nano[15]	Porous Carbon Membranes	-	-	74.69	-
2018 Small[16]	carbon nanotubes (CNTs) and fire-resistant inorganic paper	-	-	83.2	-
2019 Journal of Materials Chemistry A[17]	black gold nanoparticle-deposited sponge	-	-	80	-
2019 Nano Energy[18]	melamine-derived carbon sponges	-	-	69.7	92
2019 Advanced Materials[19]	artificial channel-array in a natural wood substrate	-	75.1	-	-
2019 Nano Energy[20]	Bio-Derived Ultrathin Membrane	-	-	75-80	-
2019 Acs Applied Materials & Interfaces[2]	hollow glass microsphere−carbon black architecture	-	-	82.1	-
2018 Energy & Environmental Science[21]	A salt-rejecting floating solar still	-	57	-	-
2017 Energy & Environmental Science[22]	a hybrid system for electricity generation	-	-	-	73
2018 Energy & Environmental Science[3]	hydrogel-based antifouling solar evaporator	-	-	95	-
2017 Environmental Science & Technology[23]	Graphene Oxide Leaf	-	-	-	80-85
2016 Proceedings of the National Academy of Sciences of the United States of America[24]	2D water paths solar evaporator	-	-	-	78-80
2017 Advanced Materials[25]	GO-based aerogels	-	-	83	-
2018 Advanced Energy Materials[26]	A flexible Janus absorber	-	-	85	-
2018 Advanced Functional Materials[27]	a geopolymer–biomass mesoporous carbon composite device	-	-	-	84.95

2018 Advanced Energy Materials[5]	3D polyurethane sponge	-	-	-	88
2014 Nature Communication[28]	A carbon foam supporting an exfoliated graphite	-	-	64	-
2017 Advanced Materials[29]	carbon nanotube (CNT)-modified flexible wood membrane (F-Wood/CNTs)	-	-	65	-
2017 Journal of Materials Chemistry A[30]	Paper-based membranes on silicone floaters	-	-	80.6	-
2019 Advanced Materials[31]	MOF-Based Hierarchical Structures	-	-	-	96
2018 Advanced Energy Materials[32]	Solar Absorber Gel (Au)	-	-	85	-
2016 Nature Energy[33]	floating structure with thermal concentration	-	-	-	~89
2018 Nano Energy[34]	defect-abundant graphene aerogel	-	-	-	91
2017 National Science Review[35]	Three-dimensional artificial transpiration	-	-	-	85
2018 Small Method[36]	Hydrophobic/Hydrophilic Bifunctional Structure	-	-	-	82
2020 Desalination[37]	printed paper-based solar absorber	-	-	-	~78% (1.1 sun)

(Notice: Text in red means literatures reporting salt-rejecting property.)

References

1. S. Wu, G. Xiong, H. Yang, B. Gong, Y. Tian, C. Xu, Y. Wang, T. Fisher, J. Yan, K. Cen, T. Luo, X. Tu, Z. Bo and K. Ostrikov, *Adv. Energy Mater.*, 2019, **0**, 1901286-1901297.
2. W. Zhang, G. Zhang, Q. Ji, H. Liu, R. Liu and J. Qu, *Acs Appl. Mater. Interfaces*, 2019, **11**, 9974-9983.
3. X. Zhou, F. Zhao, Y. Guo, Y. Zhang and G. Yu, *Energy Environ. Sci.*, 2018, **11**, 1985-1992.
4. F. Zhao, X. Zhou, Y. Shi, X. Qian, M. Alexander, X. Zhao, S. Mendez, R. Yang, L. Qu and G. Yu, *Nat. Nanotechnol.*, 2018, **13**, 489-495.
5. L. Zhu, M. Gao, C. K. N. Peh, X. Wang and G. W. Ho, *Adv. Energy Mater.*, 2018, **8**, 1702149-1702156.
6. J. Zeng, Q. Wang, Y. Shi, P. Liu and R. Chen, *Adv. Energy Mater.*, 2019, **9**.
7. L. Zhou, Y. Tan, J. Wang, W. Xu, Y. Yuan, W. Cai, S. Zhu and J. Zhu, *Nat. Photonics*, 2016, **10**, 393-398.
8. K. Bae, G. Kang, S. K. Cho, W. Park, K. Kim and W. J. Padilla, *Nat. Commun.*, 2015, **6**, 10103.
9. J. Yang, Y. Pang, W. Huang, S. K. Shaw, J. Schiffbauer, M. A. Pillers, X. Mu, S. Luo, T. Zhang and Y. Huang, *Acs Nano*, 2017, **11**, 5510-5518.
10. L. Zhou, Y. Tan, D. Ji, B. Zhu, P. Zhang, J. Xu, Q. Gan, Z. Yu and J. Zhu, *Sci. Adv.*, 2016, **2**, e1501227.
11. Y. Li, T. Gao, Z. Yang, C. Chen, W. Luo, J. Song, E. Hitz, C. Jia, Y. Zhou and B. Liu, *Adv. Mater.*, 2017, **29**, 1700981-1700988.
12. P. Mu, Z. Zhang, W. Bai, J. He, H. Sun, Z. Zhu, W. Liang and A. Li, *Adv. Energy Mater.*, 2018, **9**, 1802158-1802166.
13. N. Xu, X. Hu, W. Xu, X. Li, L. Zhou, S. Zhu and J. Zhu, *Adv. Mater.*, 2017, **29**, 1606762-1606766.
14. Y. Ito, Y. Tanabe, J. Han, T. Fujita, K. Tanigaki and M. Chen, *Adv. Mater.*, 2015, **27**, 4302-4307.
15. Y. Shao, Z. Jiang, Y. Zhang, T. Wang, P. Zhao, Z. Zhang, J. Yuan and H. Wang, *ACS Nano*, 2018, **12**, 11704-11710.
16. Z. C. Xiong, Y. J. Zhu, D. D. Qin, F. F. Chen and R. L. Yang, *Small*, 2018, **14**, e1803387-1803399.
17. Y. Liu, Z. Liu, Q. Huang, X. Liang, X. Zhou, H. Fu, Q. Wu, J. Zhang and W. Xie, *J. Mater. Chem. A*, 2019, **7**, 2581-2588.
18. F. Gong, H. Li, W. Wang, J. Huang, D. Xia, J. Liao, M. Wu and D. V. Papavassiliou, *Nano Energy*, 2019, **58**, 322-330.
19. Y. Kuang, C. Chen, S. He, E. M. Hitz, Y. Wang, W. Gan, R. Mi and L. Hu, *Adv. Mater.*, 2019, DOI: 10.1002/adma.201900498, e1900498-1900506.
20. X. Han, W. Wang, K. Zuo, L. Chen, L. Yuan, J. Liang, Q. Li, P. M. Ajayan, Y. Zhao and J. Lou, *Nano Energy*, 2019, **60**, 567-575.
21. G. Ni, S. H. Zandavi, S. M. Javid, S. V. Boriskina, T. A. Cooper and G. Chen, *Energy Environ. Sci.*, 2018, **11**, 1510-1519
22. P. Yang, K. Liu, Q. Chen, J. Li, J. Duan, G. Xue, Z. Xu, W. Xie and J. Zhou, *Energy Environ. Sci.*, 2017, **10**, 1923-1927.
23. C. Finnerty, L. Zhang, D. L. Sedlak, K. L. Nelson and B. Mi, *Environ. Sci. Technol.*, 2017, **51**, 11701–11709.
24. X. Li, W. Xu, M. Tang, L. Zhou, B. Zhu, S. Zhu and J. Zhu, *Proc. Natl. Acad. Sci. U. S. A.*, 2016, **113**, 13953-13958.
25. X. Hu, W. Xu, L. Zhou, Y. Tan, Y. Wang, S. Zhu and J. Zhu, *Adv. Mater.*, 2017, **29**, 1604031-1604035.
26. W. Xu, X. Hu, S. Zhuang, Y. Wang, X. Li, L. Zhou, S. Zhu and J. Zhu, *Adv. Energy Mater.*, 2018, **8**, 1702884-1702890.

27. F. Liu, B. Zhao, W. Wu, H. Yang, Y. Ning, Y. Lai and R. Bradley, *Adv. Funct. Mater.*, 2018, **28**, 1803266-1803276.
28. H. Ghasemi, G. Ni, A. M. Marconnet, J. Loomis, S. Yerci, N. Miljkovic and G. Chen, *Nat. Commun.*, 2014, **5**, 4449-4455.
29. C. Chen, Y. Li, J. Song, Z. Yang, Y. Kuang, E. Hitz, C. Jia, A. Gong, F. Jiang and J. Y. Zhu, *Adv. Mater.*, 2017, **29**, 1701756-1701763.
30. Z. Wang, Q. Ye, X. Liang, J. Xu, C. Chang, C. Song, W. Shang, J. Wu, P. Tao and T. Deng, *J. Mater. Chem. A*, 2017, **5**, 16359-16368.
31. Q. Ma, P. Yin, M. Zhao, Z. Luo, Y. Huang, Q. He, Y. Yu, Z. Liu, Z. Hu, B. Chen and H. Zhang, *Adv. Mater.*, 2019, DOI: 10.1002/adma.201808249, e1808249-1808256.
32. M. Gao, C. K. Peh, H. T. Phan, L. Zhu and G. W. Ho, *Adv. Energy Mater.*, 2018, **8**, 1800711-1800720.
33. G. Ni, G. Li, S. V. Boriskina, H. Li, W. Yang, T. J. Zhang and G. Chen, *Nat. Energy*, 2016, **1**, 16126-16132.
34. P. Zhang, Q. Liao, T. Zhang, H. Cheng, Y. Huang, C. Yang, C. Li, L. Jiang and L. Qu, *Nano Energy*, 2018, **46**, 415-422.
35. X. Li, R. Lin, G. Ni, N. Xu, X. Hu, B. Zhu, G. Lv, J. Li, S. Zhu and J. Zhu, *National Science Review*, 2017, **5**, 70-77.
36. T. Gao, Y. Li, C. Chen, Z. Yang, Y. Kuang, C. Jia, J. Song, E. M. Hitz, B. Liu, H. Huang, J. Yu, B. Yang and L. Hu, *Small Methods*, 2019, **3**, 1800176-1800184.
37. J. Xu, Z. Wang, C. Chang, B. Fu, P. Tao, C. Song, W. Shang and T. Deng, *Desalination*, 2020, **484**.